Low Rank Enhanced Matrix Recovery of Hybrid Time and Frequency Data in Fast Magnetic Resonance Spectroscopy

Hengfa Lu, Xinlin Zhang, Tianyu Qiu, Jian Yang, Jiaxi Ying, Di Guo, Zhong Chen, Xiaobo Qu*

***Abstract*—*Goal:* The two dimensional magnetic resonance spectroscopy (MRS) possesses many important applications in bio-engineering but suffers from long acquisition duration. Non-uniform sampling has been applied to the spatiotemporally encoded ultrafast MRS, but results in missing data in the hybrid time and frequency plane. An approach is proposed to recover this missing signal, of which enables high quality spectrum reconstruction. *Methods:* The natural exponential characteristic of MRS is exploited to recover the hybrid time and frequency signal. The reconstruction issue is formulated as a low rank enhanced Hankel matrix completion problem and is solved by a fast numerical algorithm. *Results:* Experiments on synthetic and real MRS data show that the proposed method provides faithful spectrum reconstruction, and outperforms the state-of-the-art compressed sensing approach on recovering low-intensity spectral peaks and robustness to different sampling patterns. *Conclusion:* The exponential signal property serves as an useful tool to model the time domain MRS signals and even allows missing data recovery. The proposed method has been shown to reconstruct high quality MRS spectra from non-uniformly sampled data in the hybrid time and frequency plane. *Significance:* Low-intensity signal reconstruction is generally challenging in biological MRS and we provide a solution to this problem. The proposed method may be extended to recover signals that generally can be modeled as a sum of exponential functions in biomedical engineering applications, e.g. signal enhancement, feature extraction and fast sampling.**

***Index Terms*—Fast sampling, magnetic resonance spectroscopy, exponential signal, reconstruction, low rank.**

I. Introduction

MAGNETIC resonance spectroscopy (MRS) embraces a wide range of applications in biomedical engineering, such as structural biology [1]–[3], metabolic studies [4], [5] and clinical diagnosis [6]. The one dimensional (1D) MRS, obtained by performing the 1D Fourier transform on the acquired time domain data (called free induction decay, FID), provides protein structural and dynamical information with chemical shifts, coupling constant and signal strength [7]. The two dimensional (2D) MRS is obtained by repeating a series of 1D MRS with certain delays. The dimension where the 1D experiments lies in is called direct dimension while the other dimension is named indirect dimension, as shown in Fig. 1(a). When high resolution spectrum is expected, the acquisition of 2D MRS will last in the order of minutes [8], much longer than that of 1D MRS that requires only seconds. For higher dimensional spectrum, their acquisition time may rise to hours or weeks [8]. Therefore, accelerating data acquisition constitutes an important step in MRS applications.

There are numerous approaches to reduce data acquisition time in MRS, such as new hardware designs [9], pulse sequence optimization [10]–[13] and sparse sampling [14]–[20]. Particularly, the spatiotemporally encoded ultrafast (STEU) MRS saves significant time of successive 1D experiments in the conventional 2D MRS [12], and even can be capable of real-time studies [21], [22]. This technology concurrently encodes the spectral information in the indirect dimension along spatial layers of substances in test tubes, and a 2D spectrum will be obtained in a single scan. In the direct dimension, the STEU temporally encodes time information as the conventional MRS does. This specific encoding scheme in STEU MRS results in its indirect dimension lying in the frequency domain, but not in the time domain as conventional MRS does. Then, only 1D Fourier transform is performed on the direct dimension to obtain a complete 2D spectrum [12]. The 2D STEU MRS data are acquired in a hybrid time and frequency (HTF) plane (Fig. 1(b)). The STEU MRS, however, has a demand of strong acquisition gradients, which inflicts harms to magnetic resonance instrument [23]. Recently, for the purpose of circumventing this shortcoming, the non-uniform sampling has been introduced and the acquired acquisition gradient strength can maximally decrease to 20%. However, it leads to the missing of data points on the HTF plane [23]. Then, we have to reconstruct these missing points with proper spectrum properties [14]–[18], [24]–[26] to obtain a high-resolution MRS.

Recovering missing data in the HTF plane where each data point simultaneously carries time and frequency information (Fig. 2) poses as a challenging task. Recently, compressed sensing (CS) has been applied to recover HTF signals [23]. This approach exploits the spectral sparsity of each 1D time domain signals along the direct dimension and provides nice reconstruction. However, CS provides unsatisfactory reconstruction of broad and low-intensity peaks due to the loss of

This work was supported by the National Natural Science Foundation of China (61571380, 61672335, 61601276 and U1632274), Natural Science Foundation of Fujian Province of China (2015J01346 and 2016J05205), Important Joint Research Project on Major Diseases of Xiamen City (3502Z20149032), Fundamental Research Funds for the Central Universities (20720150109). *Asterisk indicates corresponding author (Email: quxiaobo@xmu.edu.cn).*

Hengfa Lu, Xinlin Zhang, Tianyu Qiu, Jian Yang, Zhong Chen and Xiaobo Qu are with Department of Electronic Science, Fujian Provincial Key Laboratory of Plasma and Magnetic Resonance, Xiamen University, Xiamen, China.

Di Guo is with School of Computer and Information Engineering, Fujian Provincial University Key Laboratory of Internet of Things Application Technology, Xiamen University of Technology, Xiamen, China.

sparsity. In practice, the loss of weak peaks and shrinkage of broad peaks are observed in CS reconstruction [19]. These peaks, however, play indispensable role in some MRS applications, e.g. carboxylic acids [27].

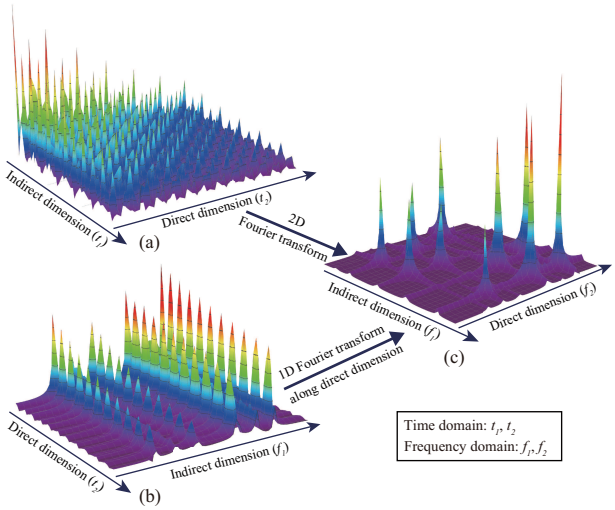

Fig. 1. An illustration of acquired 2D MRS signals using traditional and STEU methods. (a) The traditionally acquired signal in the time-time plane; (b) The STEU acquired signal in the time-frequency plane; (c) The 2D spectrum in the frequency-frequency plane.

Instead of penalizing peak intensities, the state-of-the-art low rank Hankel-matrix (LRHM) method aims to minimize the number of spectral peaks [19], and thus averts the impact of sparsity of each peak. It has been shown that LRHM is capable of reconstructing both broad and narrow peaks faithfully. The LRHM serves as a time domain reconstruction method because it explores the equivalence of (a) the rank of a Hankel matrix, constructed by a time domain MRS signal, and (b) the number of component exponentials. This property, originates from the physical modeling of MRS signals, has been applied to MRS signal processing for decades [20], [28]–[31]. However, the LRHM was originally designed for missing data recovery in the time domain, but not in the HTF planes as discussed in this article. Thus, how to explore the low rank or sparsity for HTF signals raises a challenging problem.

In this work, a new approach, simultaneously exploring the exponential structures in time and frequency dimensions, is proposed for recovering 2D HFT signals. We first convert the 2D HTF signal into a 2D time-time domain signal, and then construct an enhanced Hankel matrix. We enforce the enhanced Hankel matrix to be low-rank and design a fast algorithm without singular value decomposition (SVD). Results on synthetic and real STEU COSY spectra demonstrate that the proposed approach achieves faithful reconstruction of line shapes for spectral peaks and quantitative criteria. A preliminary account of this study was presented in a recent conference paper [32].

The remainder of this article is organized bellow. Section II describes the proposed model and the numerical algorithm. Section III first evaluates the typical reconstruction performance on synthetic and real MRS signals, and then discuss reconstructions with different sampling patterns, noise levels

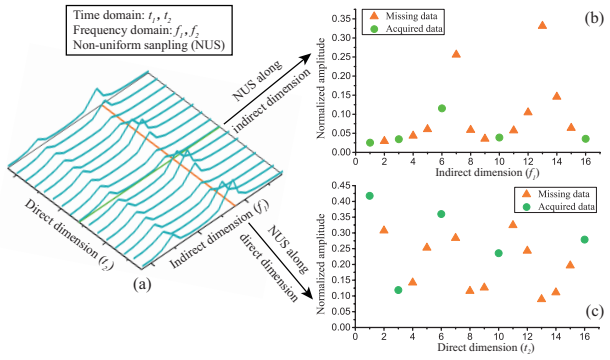

Fig. 2. Principle illustration of hybrid time-frequency plane.

and sampling rates, as well as the selection of regularization parameter λ. Section IV draws the conclusion.

II. Proposed Method

A. Challenge of spectrum recovery

The signals reconstruction along the direct dimension of STEU MRS serves as a time domain signal recovery problem. As discussed above, LRHM outperforms CS in terms of broad and low-intensity peak reconstruction [19]. In principle, the time domain exponential signal recovery by LRHM model possesses reasonability [20], [28], [31]. The LRHM allows exact recovery of 1D or 2D exponentials from noiseless time domain measurements [33] as long as the number of time domain measurements exceeds the order of $r\log^4 n$, where r and n denote the number of peaks and the ambient dimension of the signal, respectively.

In practice, both this work and our previous work in real MRS application [19] verify that the LRHM enjoys advantage over recovering the broad and low-intensity peaks compared with CS.

As a frequency domain signal recovery problem, the reconstruction of signals along the indirect dimension of STEU MRS faces challenge. To restore the frequency domain signal, we consider using CS or LRHM to reconstruct these frequency domain signals. For instance, the 1D frequency domain signal may be reconstructed by extending the ℓ_1 norm minimization [15], [16] as

$$\min_{\mathbf{s}} \|\mathbf{s}\|_1 + \frac{\lambda}{2}\|\mathbf{y}-\mathbf{P}\mathbf{s}\|_2^2, \tag{1}$$

where $\mathbf{s}$ denotes 1D frequency domain signal, $\mathbf{y}$ acquired frequency domain data and $\mathbf{P}$ the undersampling operator in frequency domain. The parameter λ balances the sparsity with the data consistency and $\|.\|_1$ and $\|.\|_2$ denote ℓ_1 (sum of absolute values) and ℓ_2 norm (the square root of the sum of the squares) of a vector, respectively. We can extend LRHM [19] to reconstruct frequency domain signals as

$$\min_{\mathbf{s}} \left\|\mathbf{Q}\mathbf{F}^{-1}\mathbf{s}\right\|_* + \frac{\lambda}{2}\|\mathbf{y}-\mathbf{P}\mathbf{s}\|_2^2, \tag{2}$$

where $\mathbf{Q}$ denotes constructing a Hankel matrix from a vector, $\|.\|_*$ the nuclear norm (sum of singular values) and $\mathbf{F}^{-1}$ inverse Fourier transform.

We have conducted a numerical experiment in Fig. 3 to validate the possibility of two approaches on frequency domain signal recovery. Figure 3 implies that LRHM provides faithful reconstruction of frequency domain signal but CS cannot. According to the CS theory, for the sake of obtaining a faithful reconstruction, the space, in which the signal is acquired, should not be the same with the space where the sparsity is enforced [34], [35]. If we perform sampling and enforce spectrum sparsity on the same signal space, the frequency information will be lost in CS reconstruction due to direct data loss in the spectrum. The LRHM takes another direction, along which the rank of the time domain signals of the spectrum is enforced. These comparisons lead us to choose LRHM to restore frequency domain signals in STEU MRS. Regarding the 2D STEU signal discussed here, it simultaneously carries time and frequency information. Therefore, a new low rank reconstruction model need to be designed.

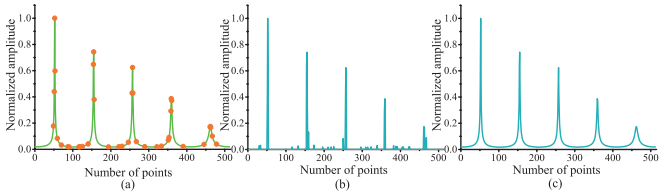

Fig. 3. Missing data recovery of spectrum. (a) The ground truth spectrum (green solid line) and acquired frequency data points (yellow dots), (b) and (c) are recovered spectrum by imposing the spectrum sparsity in CS and the low rank of time signal in LRHM, respectively. Note: The 8% spectral points are acquired from the total 512 spectral points.

In summary, the low rankness of signals along both direct and indirect dimensions should be explored to restore the hybrid time and frequency signals in STEU MRS.

B. Low Rank Enhanced Hankel Matrix of MRS Signal

The 2D MRS signal can be modeled as a sum of damped exponentials $\mathbf{X} \in \mathbb{C}^{M\times N}$ [28],

$$X_{m,n}=\sum_{r=1}^{R} a_r e^{\left(i2\pi m\Delta t_1 f_{1,r}-\frac{m\Delta t_1}{\tau_{1,r}}\right)} e^{\left(i2\pi n\Delta t_2 f_{2,r}-\frac{n\Delta t_2}{\tau_{2,r}}\right)}, \quad (3)$$

where $0 \le m < M-1$, $0 \le n < N-1$. $a_r = d_r \exp(i\phi_{1,r}+i\phi_{2,r})$ denotes the complex amplitude, $\tau_{1,r}$ and $\tau_{2,r}$ decay constants of the magnetization, $f_{1,r}$ and $f_{2,r}$ frequencies.

For simplicity, Eq. (3) is rewritten as

$$X_{m,n}=\sum_{r=1}^{R} a_r c_r^m w_r^n, \quad (4)$$

where $c_r = \exp(i2\pi\Delta t_1 f_{1,r} - \Delta t_1/\tau_{1,r})$ and $w_r = \exp(i2\pi\Delta t_2 f_{2,r} - \Delta t_2/\tau_{2,r})$.

The block Hankel matrix $\mathbf{BX} \in {}^{k_1k_2\times(N-k_2+1)(M-k_1+1)}$ is defined as [33], [36], [37]

$$\mathbf{BX}=\begin{bmatrix} \mathbf{X}_0 & \mathbf{X}_1 & \cdots & \mathbf{X}_{M-k_1} \\ \mathbf{X}_1 & \mathbf{X}_2 & \cdots & \mathbf{X}_{M-k_1+1} \\ \vdots & \vdots & \vdots & \vdots \\ \mathbf{X}_{k_1-1} & \mathbf{X}_{k_1} & \cdots & \mathbf{X}_{M-1} \end{bmatrix}, \quad (5)$$

where $\mathbf{B}$ denotes an operator that transforms a matrix to a block Hankel matrix and k_1 is called a pencil parameter [33], [36], [37]. Each submatrix $\mathbf{X}_m$ in $\mathbf{BX}$ is a Hankel matrix, satisfying

$$\mathbf{X}_m=\begin{bmatrix} X_{m,0} & X_{m,1} & \cdots & X_{m,N-k_2} \\ X_{m,1} & X_{m,2} & \cdots & X_{m,N-k_2+1} \\ \vdots & \vdots & \vdots & \vdots \\ X_{m,k_2-1} & X_{m,k_2} & \cdots & X_{m,N-1} \end{bmatrix}, \quad (6)$$

where k_2 denotes another pencil parameter [33], [36], [37].

The Hankel matrix $\mathbf{X}_m$ can be expressed as

$$\mathbf{X}_m = \mathbf{W}_L \mathbf{C}_d^m \mathbf{A} \mathbf{W}_O, \quad (7)$$

where

$$\mathbf{W}_L=\begin{bmatrix} 1 & 1 & \cdots & 1 \\ w_1 & w_2 & \cdots & w_R \\ \vdots & \vdots & \vdots & \vdots \\ w_1^{k_2-1} & w_2^{k_2-1} & \cdots & w_R^{k_2-1} \end{bmatrix}, \quad (8)$$

$$\mathbf{W}_O=\begin{bmatrix} 1 & w_1 & \cdots & w_1^{N-k_2} \\ 1 & w_2 & \cdots & w_2^{N-k_2} \\ \vdots & \vdots & \vdots & \vdots \\ 1 & w_R & \cdots & w_R^{N-k_2} \end{bmatrix}, \quad (9)$$

$$\mathbf{C}_d = \operatorname{diag}[c_1, c_2, \cdots, c_R], \quad (10)$$

$$\mathbf{A} = \operatorname{diag}[a_1, a_2, \cdots, a_R]. \quad (11)$$

Thus, combing Eq. (7) with Eq. (5), $\mathbf{BX}$ becomes

$$\mathbf{BX}=\begin{bmatrix} \mathbf{W}_L \\ \mathbf{W}_L\mathbf{C}_d \\ \vdots \\ \mathbf{W}_L\mathbf{C}_d^{k_1-1} \end{bmatrix} \mathbf{A} \left[\mathbf{W}_O, \mathbf{C}_d\mathbf{W}_O, \cdots, \mathbf{C}_d^{M-k_1}\mathbf{W}_O\right], \quad (12)$$

where the column and row space of $\mathbf{BX}$ are spanned. From Eq. (7) to Eq. (12), it has been found that [33], [36]

$$\operatorname{rank}(\mathbf{BX}) \le R, \quad (13)$$

where $\operatorname{rank}(\mathbf{BX}) = R$ if and only if each pair (c_r, w_r) is distinct.

Thus, $\mathbf{BX}$ meets low rank based on the assumption that the number of the spectral peaks satisfies the condition $R \ll min\{k_1k_2, (N-k_2+1)(M-k_1+1)\}$. Fortunately, in the field of MRS, the assumption above is generally satisfied [19], implying that the low rank property can be applied in MRS reconstruction.

C. Signal Reconstruction Model

The fully sampled 2D signal from the spectrometer in STEU is denoted as a matrix $\mathbf{G}$ (Fig. 2(a)), where each row of $\mathbf{G}$ serves as a frequency domain signal (in the indirect dimension) while each column of $\mathbf{G}$ denotes a time domain signal (in the direct dimension), respectively. The operator $\mathbf{F}_{freq}^{-1}$ denotes converting each row of a HTF signal into a time domain signal by performing inverse 1D discrete Fourier transform, and thus

$\mathbf{F}_{freq}^{-1}\mathbf{G}$ poses as a 2D time domain signal. Then this 2D signal is transformed into an enhanced matrix that is low rank.

In this work, we propose the following low rank reconstruction model to restore HTF signals:

$$\min_{\mathbf{G}} \left\|\mathbf{B}\mathbf{F}_{freq}^{-1}\mathbf{G}\right\|_* + \frac{\lambda}{2}\left\|\mathbf{Y}-\mathbf{P}_\Omega\mathbf{G}\right\|_F^2, \tag{14}$$

where $\mathbf{Y}$ denotes acquired HTF data with zeros filling on non-acquired data points, $\mathbf{P}_\Omega$ the operator that performs undersampling on 2D signal with zeros filling on non-acquired data points and $\|.\|_F$ the Frobenius norm (the square root of the sum of the squares) of a matrix. The parameter λ tradeoffs between the nuclear norm term $\left\|\mathbf{B}\mathbf{F}_{freq}^{-1}\mathbf{G}\right\|_*$ and data consistency term $\|\mathbf{Y}-\mathbf{P}_\Omega\mathbf{G}\|_F^2$. Fundamentally, we are looking for a 2D spectrum with minimal number of peaks subject to the acquired data. The proposed model is also an extension of CS because the nuclear norm can be considered a special case of ℓ_1 norm in the sense of the sum of the absolute of singular values. However, in order to distinguish the proposed method from previous CS method that minimizes the ℓ_1 norm of spectrum [23], we consistently use low rank in the rest of this paper to interpret our work.

Matrix completion can be obtained by nuclear norm minimization, and SVD is typically required for the singular value thresholding operator [38]. However, it is time and memory consuming to perform SVD on a large scale matrix. For example, given a 256×256 matrix $\mathbf{X}$, the size of its block Hankel matrix $\mathbf{B}\mathbf{X}$ will reach 16384×16641 with pencil parameters $k_1 = 128$, $k_2 = 128$. Performing one-time SVD on this matrix will take nearly half an hour on our computing server equipped with 112 GB memory and two physical CPUs at 3.5 GHz. It will spend hours on performing SVD in iterative algorithm [19], preventing its application in practical MRS reconstruction. A number of strategies have been proposed to reduce the cost of performing SVD on a large scale matrix [39]–[41]. But, in this paper, a SVD-free algorithm is expected to save the computation for the low rank reconstruction. It has been shown that the following relationship holds true [42]

$$\|\mathbf{X}\|_* = \min_{\mathbf{U},\mathbf{V}} \frac{1}{2}\left(\|\mathbf{U}\|_F^2 + \|\mathbf{V}\|_F^2\right) \quad s.t. \quad \mathbf{U}\mathbf{V}^H = \mathbf{X}, \tag{15}$$

where $\mathbf{U}$ and $\mathbf{V}$ denotes two matrices and the upper subscript H denotes Hermitian transpose of a matrix. With this proxy, SVD computation is no longer required since only Frobenius norm and matrix factorizations are involved.

Therefore, we further propose the equivalent SVD-free reconstruction model

$$\begin{aligned}\min_{\mathbf{G},\mathbf{U},\mathbf{V}} \frac{1}{2}\left(\|\mathbf{U}\|_F^2 + \|\mathbf{V}\|_F^2\right) + \frac{\lambda}{2}\|\mathbf{Y}-\mathbf{P}_\Omega\mathbf{G}\|_F^2 \\ s.t. \quad \mathbf{U}\mathbf{V}^H = \mathbf{B}\mathbf{F}_{freq}^{-1}\mathbf{G}\end{aligned} \tag{16}$$

to restore HTF signals. This model avoids SVD computation, thus the computational complexity reduces significantly. We call the proposed model as low rank block Hankel matrix of hybrid time and frequency signals (LRBHM-HTF).

D. Numerical Algorithm

In this subsection, we design an efficient numerical algorithm to solve the proposed model in Eq. (16). For the sake of obtaining fast computation in low rank reconstruction, the alternating direction method of multipliers algorithm [19], [20], [43], [44] is modified to fit the reconstruction problem here. The main steps are derived below.

The augmented Lagrangian form of Eq. (16) is

$$\begin{aligned}\max_{\mathbf{D}} \min_{\mathbf{G},\mathbf{U},\mathbf{V}} \frac{1}{2}\|\mathbf{U}\|_F^2 + \frac{1}{2}\|\mathbf{V}\|_F^2 + \left\langle \mathbf{D}, \mathbf{B}\mathbf{F}_{freq}^{-1}\mathbf{G} - \mathbf{U}\mathbf{V}^H\right\rangle \\ + \frac{\beta}{2}\left\|\mathbf{B}\mathbf{F}_{freq}^{-1}\mathbf{G} - \mathbf{U}\mathbf{V}^H\right\|_F^2 + \frac{\lambda}{2}\|\mathbf{Y}-\mathbf{P}_\Omega\mathbf{G}\|_F^2,\end{aligned} \tag{17}$$

where $\mathbf{D}$ denotes Lagrange multiplier, $\langle\cdot,\cdot\rangle$ represents an inner product in the Hilbert space of complex matrices, defined by $\langle\mathbf{A},\mathbf{B}\rangle = \Re\langle\mathbf{A}(:),\mathbf{B}(:)\rangle = \Re(trac(\mathbf{A}^*\mathbf{B}))$, $\Re$ denotes the real part and the parameter $\beta > 0$.

To solve Eq. (17), we alternately solve the following subproblems:

$$\begin{aligned}\min_{\mathbf{G}} \frac{\lambda}{2}\|\mathbf{Y}-\mathbf{P}_\Omega\mathbf{G}\|_F^2 + \left\langle \mathbf{D}, \mathbf{B}\mathbf{F}_{freq}^{-1}\mathbf{G} - \mathbf{U}\mathbf{V}^H\right\rangle \\ + \frac{\beta}{2}\left\|\mathbf{B}\mathbf{F}_{freq}^{-1}\mathbf{G} - \mathbf{U}\mathbf{V}^H\right\|_F^2,\end{aligned} \tag{18}$$

$$\begin{aligned}\min_{\mathbf{U}} \frac{1}{2}\|\mathbf{U}\|_F^2 + \left\langle \mathbf{D}, \mathbf{B}\mathbf{F}_{freq}^{-1}\mathbf{G} - \mathbf{U}\mathbf{V}^H\right\rangle \\ + \frac{\beta}{2}\left\|\mathbf{B}\mathbf{F}_{freq}^{-1}\mathbf{G} - \mathbf{U}\mathbf{V}^H\right\|_F^2,\end{aligned} \tag{19}$$

$$\begin{aligned}\min_{\mathbf{V}} \frac{1}{2}\|\mathbf{V}\|_F^2 + \left\langle \mathbf{D}, \mathbf{B}\mathbf{F}_{freq}^{-1}\mathbf{G} - \mathbf{U}\mathbf{V}^H\right\rangle \\ + \frac{\beta}{2}\left\|\mathbf{B}\mathbf{F}_{freq}^{-1}\mathbf{G} - \mathbf{U}\mathbf{V}^H\right\|_F^2,\end{aligned} \tag{20}$$

$$\mathbf{D} \leftarrow \mathbf{D} + \tau\left(\mathbf{B}\mathbf{F}_{freq}^{-1}\mathbf{G} - \mathbf{U}\mathbf{V}^H\right), \tag{21}$$

where τ denotes the step size.

The problem (18) is equivalent to

$$\min_{\mathbf{G}} \frac{\beta}{2}\left\|\mathbf{B}\mathbf{F}_{freq}^{-1}\mathbf{G} - \mathbf{U}\mathbf{V}^H + \frac{\mathbf{D}}{\beta}\right\|_F^2 + \frac{\lambda}{2}\|\mathbf{Y}-\mathbf{P}_\Omega\mathbf{G}\|_F^2, \tag{22}$$

whose solution is

$$\begin{aligned}\mathbf{G} = &\left(\lambda\mathbf{P}_\Omega^H\mathbf{P}_\Omega + \beta\mathbf{F}_{freq}\mathbf{B}^H\mathbf{B}\mathbf{F}_{freq}^{-1}\right)^{-1} \\ &\left[\lambda\mathbf{P}_\Omega^H\mathbf{Y} + \beta\mathbf{F}_{freq}\mathbf{B}^H\left(\mathbf{U}\mathbf{V}^H - \frac{\mathbf{D}}{\beta}\right)\right].\end{aligned} \tag{23}$$

For problem (19), we have

$$\min_{\mathbf{U}} \frac{1}{2}\|\mathbf{U}\|_F^2 + \frac{\beta}{2}\left\|\mathbf{B}\mathbf{F}_{freq}^{-1}\mathbf{G} - \mathbf{U}\mathbf{V}^H + \frac{\mathbf{D}}{\beta}\right\|_F^2, \tag{24}$$

and its solution is

$$\mathbf{U} = \left(\beta\mathbf{B}\mathbf{F}_{freq}^{-1}\mathbf{G} + \mathbf{D}\right)\mathbf{V}\left(\beta\mathbf{V}^H\mathbf{V} + \mathbf{I}\right)^{-1}. \tag{25}$$

The problem (20) can be expressed as

$$\min_{\mathbf{V}} \frac{1}{2}\|\mathbf{V}\|_F^2 + \frac{\beta}{2}\left\|\mathbf{B}\mathbf{F}_{freq}^{-1}\mathbf{G} - \mathbf{U}\mathbf{V}^H + \frac{\mathbf{D}}{\beta}\right\|_F^2, \tag{26}$$

and its solution is

$$\mathbf{V} = \left(\beta \mathbf{B}\mathbf{F}_{freq}^{-1}\mathbf{G} + \mathbf{D}\right)^H \mathbf{U}\left(\beta \mathbf{U}^H\mathbf{U} + \mathbf{I}\right)^{-1}. \quad (27)$$

The problem (21) can be solved with a simple update on the dual variable $\mathbf{D}$.

The whole algorithm is summarized in Algorithm 1. In our implementation, we initialize $\mathbf{G}_0$ by the acquired hybrid time and frequency signal with zero-filling on non-acquired data points. What is more, $\mathbf{U}_0$ and $\mathbf{V}_0$ are empirically set as the matrices with random numbers that are drawn from the normal distribution with the mean 0 and the variance 1. The in-house program runs on a computer server equipped with two physical Intel Xeon CPUs (3.5 GHz) and 112 GB memory. Approximately 1 minute is required by the proposed method for the reconstruction of a typical hybrid time and frequency MRS signal in the size of 64×64.

Algorithm 1 Hybrid time and frequency signal recovery with LRBHM-HTF

Input: $\mathbf{Y}$, λ and sampling pattern.
Initialization: $k = 0$.
Output: $\mathbf{G}$.

1: **while** $k < 100$ and $\|\mathbf{G}_{k+1} - \mathbf{G}_k\|_F / \|\mathbf{G}_k\|_F \leq 5 \times 10^{-3}$ **do**

2: $$\mathbf{G}_{k+1} = \left(\lambda \mathbf{P}_\Omega^H \mathbf{P}_\Omega + \beta \mathbf{F}_{freq}\mathbf{B}^H\mathbf{B}\mathbf{F}_{freq}^{-1}\right)^{-1} \left[\lambda \mathbf{P}_\Omega^H \mathbf{Y} + \beta \mathbf{F}_{freq}\mathbf{B}^H\left(\mathbf{U}_k(\mathbf{V}_k)^H - \frac{\mathbf{D}_k}{\beta}\right)\right];$$

3: $$\mathbf{U}_{k+1} = \left(\beta \mathbf{B}\mathbf{F}_{freq}^{-1}\mathbf{G}_{k+1} + \mathbf{D}_k\right)\mathbf{V}_k \left(\beta(\mathbf{V}_k)^H\mathbf{V}_k + \mathbf{I}\right)^{-1};$$

4: $$\mathbf{V}_{k+1} = \left(\beta \mathbf{B}\mathbf{F}_{freq}^{-1}\mathbf{G}_{k+1} + \mathbf{D}_k\right)^H \mathbf{U}_{k+1} \left(\beta(\mathbf{U}_{k+1})^H\mathbf{U}_{k+1} + \mathbf{I}\right)^{-1};$$

5: $\mathbf{D}_{k+1} \leftarrow \mathbf{D}_k + \tau\left(\mathbf{B}\mathbf{F}_{freq}^{-1}\mathbf{G}_{k+1} - \mathbf{U}_{k+1}(\mathbf{V}_{k+1})^H\right)$;

6: $k = k + 1$;

7: **end while**

III. Experimental Results

In this section, typical reconstructions on synthetic and real 2D STEU MRS are carried out to validate the performance of the proposed method. Furthermore, we discuss reconstructions with different sampling patterns, noise levels and sampling rates, as well as the selection of regularization parameter λ. The 1D Poisson Gap sampling [45] along frequency axis is adopted to emulate the non-uniform sampling. In real applications, the gradient-switching based sampling pattern [23] generated according to STEU technology is obtained, which will be discussed below in III-C. The proposed LRBHM-HTF method is compared with the state-of-the-art CS method [23].

A. Typical Reconstruction of Synthetic Data

We first simulate a 2D time domain signal $\mathbf{X}$ with size 64×64 according to Eq. (3). Parameters are set as $R = 10$ and $a_r = 1$, $\phi_{1,r} = \phi_{2,r} = 0$, $\Delta t_1 = \Delta t_2 = 1$ for all $r = 1, \cdots, R$. Other parameters τ and f are listed in Table I. A 2D spectrum with 10 peaks (Fig. 4(d)) is obtained by performing 2D discrete Fourier transform on the synthetic time domain signal $\mathbf{X}$. The HTF signal (Fig. 4(a)) is first obtained by performing the 1D discrete Fourier transform on each row of $\mathbf{X}$. Then, the complex Gaussian noise whose real and imaginary part share the standard deviation $\sigma = 0.01$ are added to the HTF signal. The noisy HTF signal is then subsampled according to a Poisson Gap mask (Fig. 4(b)). The acquired noisy HTF signal is shown in Fig. 4(c).

TABLE I
Value of parameters τ and ω of the spectrum in Fig. (4)(d)

R	1	2	3	4	5
$f_{1,r}, f_{2,r}$	0.8,0.3	0.2,0.2	0.4,0.4	0.2,0.4	0.4,0.2
$\tau_{1,r}, \tau_{2,r}$	30,30	40,40	40,40	40,40	40,40
R	6	7	8	9	10
$f_{1,r}, f_{2,r}$	0.1,0.7	0.8,0.8	0.6,0.8	0.8,0.6	0.6,0.6
$\tau_{1,r}, \tau_{2,r}$	60,60	100,100	100,100	100,100	100,100

Note: Values of f have been normalized to a range of [0,1].

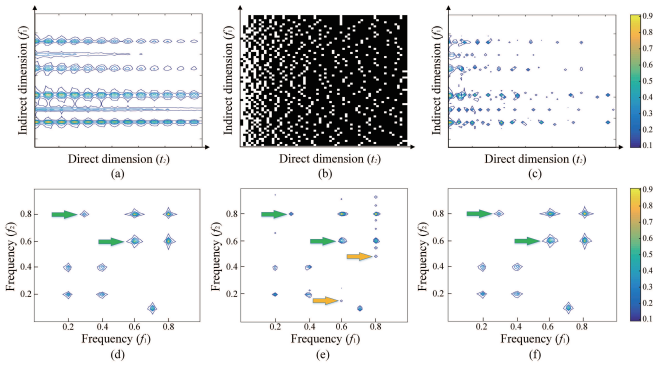

Fig. 4. Reconstruction of the synthetic spectrum. (a) denotes the full synthetic HTF signal, (b) Poisson Gap sampling mask with 20% acquired data, in which white (black) points denote sampled (non-sampled) points, (c) the acquired HTF signal according to mask in (b), (d) the synthetic spectrum, (e) and (f) are restored spectrum using CS and the proposed method. Note: The intensities of all spectra are normalized to a range from zero to one through diving intensities by the maximum amplitude. Ten contour levels with linear values are set for all spectra. The regularization parameter $\lambda = 10^5$, pencil parameters $k_1 = k_2 = 32$ and the matrices $\mathbf{U}$ and $\mathbf{V}$ are initialized as random matrix with the size of 1024×409 and 1089×409, respectively, for the proposed method.

Figure 4 shows the reconstructed spectra of synthetic data. The CS introduces some artifacts (the yellow arrows in Fig. 4(e)) and shrinkage of peaks (the green arrows in Fig. 4(e)) while the proposed method faithfully reconstructs all peaks (Fig. 4(f)). The new method has also increased the peak intensities correlation coefficient from 0.91 to 0.99 (Fig. 6), implying that the LRBHM-HTF provides more accurate spectrum reconstruction than CS.

B. Typical Reconstruction of Real NMR Data

A 2D STEU correlation spectroscopy (COSY) of a special oil is used to validate the proposed method. This kind of oil exists in intrahepatic fat of liver, and measuring it through MRS serves as an important tool for clinical trials and observational studies [4]. The STEU experiments are carried out on a Varian

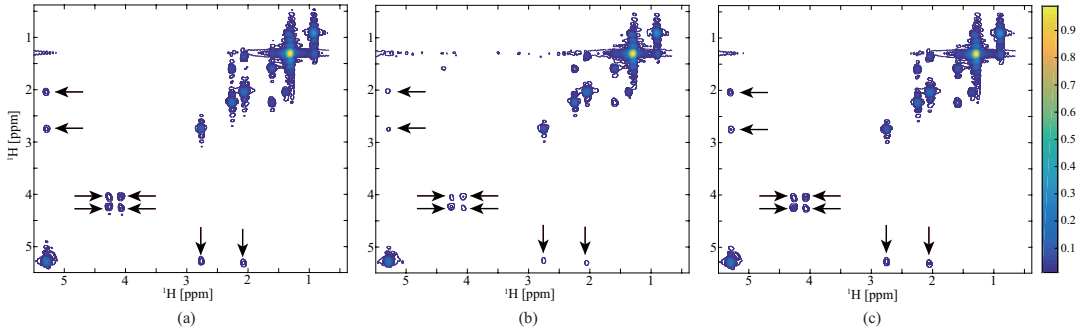

Fig. 5. Reconstruction of STEU COSY spectrum. (a) The full sampled STEU COSY spectrum; (b) The reconstructed spectrum by CS; (c) The reconstructed spectrum by proposed method. Note: All spectra are plotted in a contour level of 90. The regularization parameter $\lambda = 10^5$, pencil parameters $k_1 = 400$, $k_2 = 50$ and the matrices $\mathbf{U}$ and $\mathbf{V}$ are initialized as random matrix with the size of 20000×8000 and 20451×8000, respectively, for the proposed method.

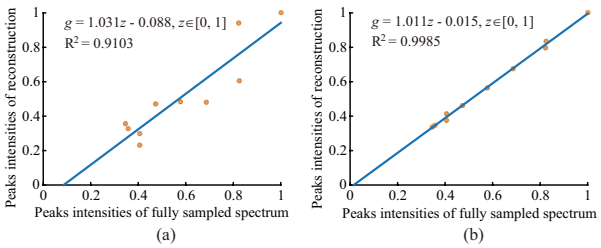

Fig. 6. Peak intensities correlation between the ground-truth spectrum and the reconstructed spectrum on synthetic data. (a) and (b) are correlation evaluation for CS and the proposed method, respectively. The formula $g = az + b$ denotes the fitted curve (see blue line) according to peak intensities between ground-truth and reconstructed spectra with a polynomial. The notation R^2 denotes Pearsons linear correlation coefficient of fitted curve. The closer that the value of R^2 gets to 1, the stronger the correlation between ground-truth and reconstructed spectra is. Note: The intensities of all spectra are normalized to a range of zero to one through diving intensities by the maximum absolute amplitude. Only the maximum intensity of each peak is included in the analysis of correlation evaluation.

500 MHz NMR System (Agilent Technologies, Santa Clara, CA, USA) equipped with a 5-mm indirect detection probe. Acquisition parameters include: encoding gradients $= 3.91$ G/cm, decoding gradients $= 48.8$ G/m, compensative gradient $= -7.81$ G/cm, duration of each decoding gradient lobe $= 220$ us, duration of the chirp pulse $= 12$ ms, duration of compensative gradient $= 0.5$ ms, and number of alternating gradient pairs $= 150$. The WURST profile with the sweep frequency range of 30 KHz in 6 ms. In real MRS applications, the unit of chemical shift is usually expressed in part per million (ppm) instead of the common Hz, to avoid ambiguity when spectrometers are at different magnet strengths. The chemical shift is defined as

$$\text{chemical shift(ppm)} = \frac{f_{\text{test}} - f_{\text{ref}}}{f_{\text{spec}}} \times 10^6, \qquad (28)$$

where f_{test} denotes resonance frequency of the sample, f_{ref} the absolute resonance frequency of a standard compound measured in the same magnetic filed and f_{spec} the frequency of magnetic field strength of spectrometer.

The acquired fully sampled 2D STEU COSY signal reaches the size of 800×100, along which the first dimension (800 data points) lies in frequency domain while the other in time domain. The fully sampled 2D spectrum is shown in Fig. 5(a). Its hybrid time and frequency signal is subsampled with a Poisson Gap sampling pattern and only 20% data points are used in reconstruction.

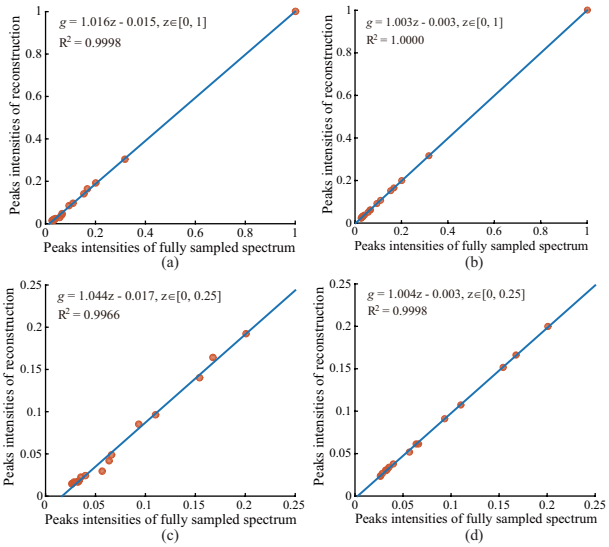

Fig. 7. Peak intensities correlation between ground-truth spectrum and reconstructed spectrum on STEU COSY. (a) and (b) are peak intensities correlations with all peaks included for CS and the proposed methods, respectively; (c) and (d) are peak intensities correlations, of which only those peaks whose amplitudes at a range of [0,0.25] are included, for CS and the proposed method, respectively. Note: The fitted curve and linear correlation coefficient are evaluated following the same way used in Fig. 6.

Figure 5 shows the reconstructed STEU spectrum. Eight low-intensity peaks are weaken or missed in CS reconstruction (see arrows in Fig. 5(b)). In contrast, these low-intensity peaks are reconstructed much better using the proposed method meanwhile other peaks are still reconstructed very well. The values of Pearsons linear correlation coefficient R^2 of CS and the proposed method are close to 1 when all peak intensities are included in regression statistics (Fig. 7(a) and (b)), which implies that both CS and the proposed method provide nice reconstructions. However, when focusing on low-intensity peaks (at a range of 0 to 0.25), we observe that the values of R^2 of CS method drops to 0.9966, but the value of R^2 of proposed method remains 0.9998 (Fig. 7(c) and (d)). The R^2 value implies that the proposed method produces more consistent reconstruction for low-intensity peaks (Fig. 5(c)) than CS (Fig. 5(b)).

Quantification of the liver fat spectrum is marked as an important tool in bio-engineering applications [4], [46]. The resonance volume is adopted as the criteria because resonance volumes of protons reflect the ratio of different components in the intrahepatic fat, which earns importance in diagnosis of liver disease [4]. The resonance volumes of the STEU COSY, discussed above, are sorted in descending order and the quantitative results are listed in Table II. Quantitative results show that proton resonance volumes in reconstructed spectrum by the proposed method are more closer to the resonance volumes in reference spectrum than CS. For better visualization of quantitative analysis in Table II, we define quantitative error factor (QEF) by

$$\text{QEF} = \frac{|\mathrm{s} - \widehat{\mathrm{s}}|}{\mathrm{s}}, \tag{29}$$

where s denotes resonance volume of proton in reference spectrum, $\widehat{\mathrm{s}}$ the resonance volume of proton in reconstructed spectra. The smaller the value of QEF is, the higher the quantification accuracy of reconstructed spectrum is. Figure 8 depicts the values of QEF according to Table II. For most high-intensity peaks (protons 2,3,4), both CS and the proposed method produce nice reconstruction, in which the QEF is lower than 0.05. However, for low-intensity peaks (protons 5 to 9), CS provides inferior result (QEF > 0.1) than the proposed method (QEF < 0.05), where the latter implies the faithful reconstruction for low-intensity peaks. Although the proton 1 is in large intensity, the CS reconstruction abnormally leads to relatively high quantitative error (QEF ≈ 0.07). Furthermore, the error bars in Fig. 8 imply that the LRBHM-HTF method is more robust to the Poisson Gap sampling pattern since the QEF values do not differ greatly under different Poisson Gap sampling patterns.

TABLE II
QUANTITATIVE ANALYSIS OF STEU COSY

Protons			Resonance volume		
ID	Type	ppm	Reference	CS	Proposed
1	methylene	1.30	37.69	40.30±0.13	38.01±0.03
2	methyl	0.90	16.79	16.73±0.15	16.80±0.02
3	olefinic	5.29	12.98	12.92±0.20	13.00±0.01
4	α-olefinic	2.02	12.08	11.79±0.16	12.06±0.03
5	α-carboxyl	2.24	8.16	7.69±0.18	8.12±0.04
6	diacyl methylene	2.75	5.23	4.64±0.11	5.17±0.03
7	β-carboxyl	1.60	4.78	4.28±0.18	4.63±0.02
8	glycerol backbone CH	4.30	1.19	0.86±0.04	1.16±0.01
9	CH_2	4.05	1.10	0.79±0.02	1.05±0.01

Note: Spectral peaks in STEU COSY are assigned to protons according to previous work [4]. Resonance volume was obtained by peak intensities of a proton dividing by the summation of peak intensities of all protons. Average resonance volumes and its corresponding standard deviation are obtained over 10 Monte Carlo trials with different sampling patterns in CS and the proposed method. The resonance volumes are normalized by the total resonance volumes.

C. Reconstructions with Different Sampling Patterns

In order to evaluate the robustness of proposed method to different sampling patterns, we adopt gradient switching-based, Poisson Gap and fully random sampling patterns. In real applications, the gradient switching-based sampling pattern is achievable and generated according to STEU technology [23] with a pseudo random oscillating gradient whose wavenumber k is obtained according to

$$k = \int_0^t \gamma_a G_a \left(t^{'}\right) dt^{'}, \tag{30}$$

where t denotes the pulse duration, γ_a the gyromagnetic ratio and G_a the acquisition gradient. The gradient switching-based sampling pattern is obtained by rearranging data points of the acquisition trajectories (in $k-t$ plane, i.e., HTF plane) into a data matrix (800×100), in which positions of sampled data points set as 1 while positions of non-sampled data points set as 0.

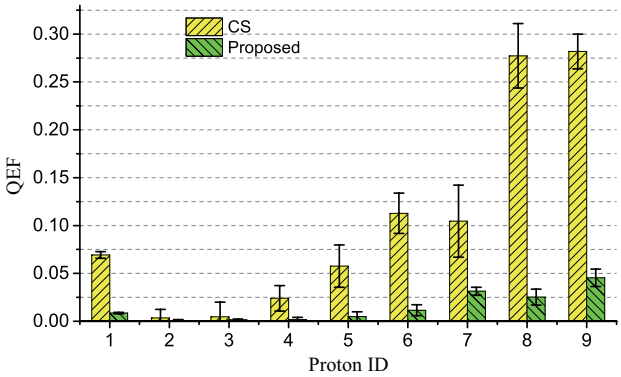

Fig. 8. QEF according to Table II. The error bars represent the deviation of the QEF under different sampling patterns.

Under three different types of sampling pattern with a fixed sampling rate of 0.5, Fig. 9 indicates that the proposed method is robust to the sampling pattern while CS is not. Given a Poisson Gap sampling pattern, CS provides as good reconstruction as the proposed approach on most peaks (see Fig. 9 (c) and (f)), but CS produces line shape shrinkage of low-intensity peaks while proposed method allows faithful reconstruction (see Fig. 9 (k)). Under both gradient switching-based and fully random sampling patterns, some low-intensity peaks are weaken or even missing in CS reconstructions (see black arrows in Fig. 9 (d) and (e)), while those peaks are reconstructed much better by the proposed method (see black arrows in Fig. 9 (g) and (h)).

D. Reconstructions under Different Noise Levels

We adopt the synthetic data with different noise levels to analyze the impact of noise level on reconstructions. Three different noise levels with $\sigma = 0.005$, 0.05 and 0.1 are used to evaluate reconstructions by CS and the proposed method.

Figure 10 indicates that under low ($\sigma = 0.005$) and moderate ($\sigma = 0.05$) noise levels, the proposed method outperforms CS in terms of spectrum reconstructions but under a high noise level ($\sigma = 0.1$), both CS and proposed method are unable to provide promising reconstructions. For example, under a low noise level ($\sigma = 0.005$), the proposed method provides faithful reconstruction while CS imposes shrinkage of peaks and introduces artifacts in reconstructions (see Fig. 10 (g) and (j)). We measure the noise of the real STEU MRS used in this work and found its noise level is 0.005. Thus, the proposed method works well for the real MRS data.

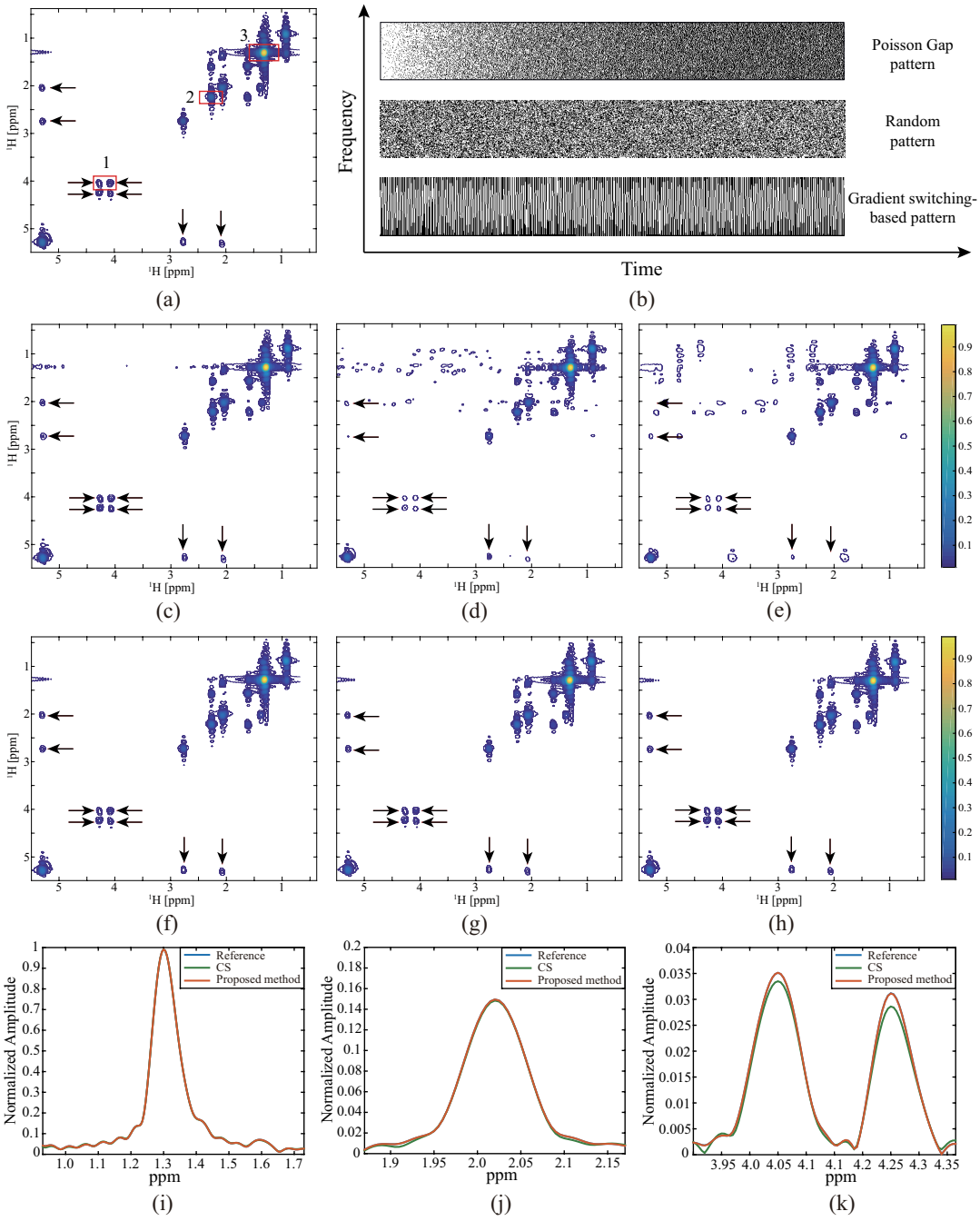

Fig. 9. Reconstructions of STEU COSY spectrum using different sampling patterns. (a) The fully sampled spectrum; (b) shows three sampling patterns with sampling rate 0.5; (c), (d) and (e) are the reconstructions by CS with Poisson Gap, random and gradient switching-based sampling patterns, respectively; (f), (g) and (h) are the reconstructions by the proposed method with Poisson Gap, random and gradient switching-based sampling patterns, respectively; (i), (j) and (k) are spectral line shapes of representative peaks #3, #2 and #1 (see (a) for peak positions) in (c) and (f). Note: The three peaks are with high, moderate and low intensities, respectively. The white points in sampling patterns denote the sampled data points while the black points denote the unsampled data points. The regularization parameter λ for the proposed method is $\lambda = 10^7$.

However, if one encounters much higher noise level $\sigma = 0.1$ in some applications, peaks may be weakened seriously in CS reconstruction and some artifacts are introduced by the proposed method (see Fig. 10 (i) and (l)). Thus, recovering the hybrid time and frequency signal under a high noise level poses as a challenging task.

E. Reconstructions with Different Sampling Rates

Under different sampling rates of gradient switching-based sampling patterns, Fig. 11 shows that the proposed method provides better reconstructions for real STEU COSY spectrum than CS. Specifically, under a sampling rate of 0.5, the proposed method allows reliable reconstruction of spectral peaks (see Fig. 11 (h) and (k)), while the CS method shows obvious line shape shrinkage of moderate and low-intensity peaks (see Fig. 11 (e) and (k)). Furthermore, under lower

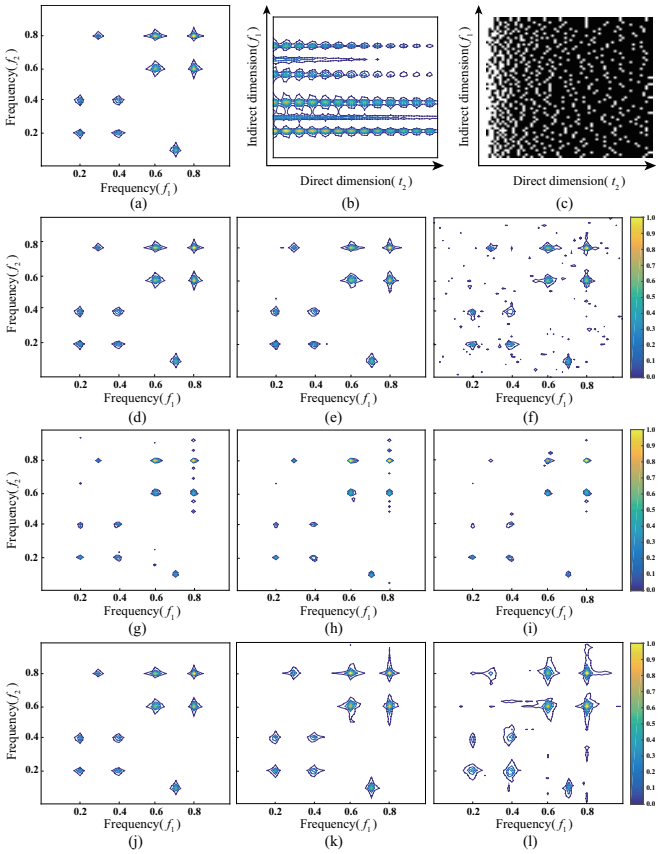

Fig. 10. Reconstructions of synthetic spectra under different noise levels. (a) denotes the noiseless fully sampled synthetic spectrum, (b) the hybrid time and frequency plane signal, (c) the corresponding sampling pattern, (d), (e) and (f) are noisy fully sampled spectra under noise levels $\sigma = 0.005$, 0.05 and 0.1, (g), (h) and (i) are reconstructions by CS under noise level $\sigma = 0.005$, 0.05 and 0.1, respectively. (j), (k) and (l) are reconstructions by proposed method under noise level $\sigma = 0.005$, 0.05 and 0.1, respectively. Note: The synthetic data in Fig. 4 (d) is used. The Poisson Gap sampling is adopted with sampling rate of 0.2.

sampling rate (sampling rate = 0.4), the proposed method is still able to keep these peaks robust (see Fig. 11 (g)) while some low-intensity peaks are weakened or even missing in CS reconstruction (see Fig. 11 (d)).

F. Selection of Regularization Parameter λ

The synthetic data (see Fig. 12(b)) with five peaks is generated according to Eq. (3) for discussing the selection of regularization parameter λ. Parameters of the synthetic data are set as $R = 5$, $a_r = 1$, $\phi_{1,r} = \phi_{2,r} = 0$ and $\Delta t_1 = \Delta t_2 = 1$ us for all $r = 1, \cdots, R$. Other parameters τ and f are listed in Table III.

To evaluate the reconstruction error, we adopt the Relative Least Normalized Error (RLNE) defined as

$$\text{RLNE} = \frac{\|\mathbf{G}_{\text{ref}} - \mathbf{G}_{\text{rec}}\|_F}{\|\mathbf{G}_{\text{ref}}\|_F} \tag{31}$$

where $\mathbf{G}_{\text{ref}}$ and $\mathbf{G}_{\text{rec}}$ denote the fully sampled signal and the reconstructed signal, respectively.

The optimal λ, producing the lowest RLNE, generally decreases as the noise level increases. For instance, as shown in Fig. 12 (a) the optimal range is $\lambda \in \left[5 \times 10^2, 10^7\right]$ for low noise level ($\sigma = 0.005$) while this range reduces to $\lambda \in \left[5 \times 10^2, 10^3\right]$ as noise level rises ($\sigma = 0.05$). Thus, a smaller λ is suitable for higher noise level.

Figure 12 (a) indicates that there exists an available range of λ ($5 \times 10^2 \leq \lambda \leq 5 \times 10^3$) that leads to a relatively low reconstruction errors. In addition, the small or large value of λ ($\lambda < 5 \times 10^2$ or $\lambda > 5 \times 10^3$) introduces higher reconstruction errors, because that a small λ results in baseline distortion (see Fig. 12 (c)) while a too large λ introduces noise into spectrum (see Fig. 12 (e)).

TABLE III
VALUE OF PARAMETERS τ AND f OF THE SPECTRUM IN Fig (12)(b)

R	1	2	3	4	5
$f_{1,r}, f_{2,r}$	0.1,0.6	0.44,0.55	0.55,0.24	0.72,0.83	0.85,0.85
$\tau_{1,r}, \tau_{2,r}$	180,200	150,150	250,250	230,230	300,300

Note: Values of f have been normalized to a range of [0,1].

IV. CONCLUSION

A low rank enhanced Hankel matrix method is proposed to reconstruct missing data in the hybrid time and frequency plane. This method is verified by the non-uniformly sampled data recovery in the spatiotemporally encoded ultrafast magnetic resonance spectroscopy. Experiments on synthetic and real magnetic resonance spectroscopy data demonstrate that the proposed approach provides faithful spectrum reconstruction and outperforms the state-of-the-art compressed sensing method in terms of reconstructing low-intensity spectral peaks and robustness to different non-uniformly sampling patterns.

We have observed that the low rank Hankel matrix approach is capable of recovering the lost spectrum data but the compared CS method is not. The proposed method primarily relies on two signal properties: 1) A limited number of peaks exists in spectrum, i.e. the spectrum is sparse; 2) The signal can be modeled or approximated by a superposition of exponential signals. Thus, the proposed method is not limited to reconstruct magnetic resonance spectroscopy but holds the potential to recover any signals in biomedical engineering applications, along which the signal is modeled by a sum of exponential functions, for example, magnetic resonance signal enhancement [20], [29], [31], [47], [48] and fast imaging [44], [49]–[51]. The code and data of this paper will be available at http://www.quxiaobo.org/project/LowRank_Hankel_HTF/Toolbox_HTF_Hankel_NMR.zip.

ACKNOWLEDGMENTS

The authors are grateful to Yanqin Lin for valuable discussion on spatiotemporally encoded ultrafast sequence, Lucio Frydman for sharing codes of compressed sensing spatiotemporally encoded magnetic resonance spectroscopy and Tien-Mo Shih for polishing writing. The authors also thank the editors and reviewers for their constructive comments.

REFERENCES

[1] T. E. Machonkin *et al.*, "^{13}C{^{13}C} 2D NMR: A novel strategy for the study of paramagnetic proteins with slow electronic relaxation rates," *Journal of the American Chemical Society*, vol. 124, no. 13, pp. 3204–3205, 2002.

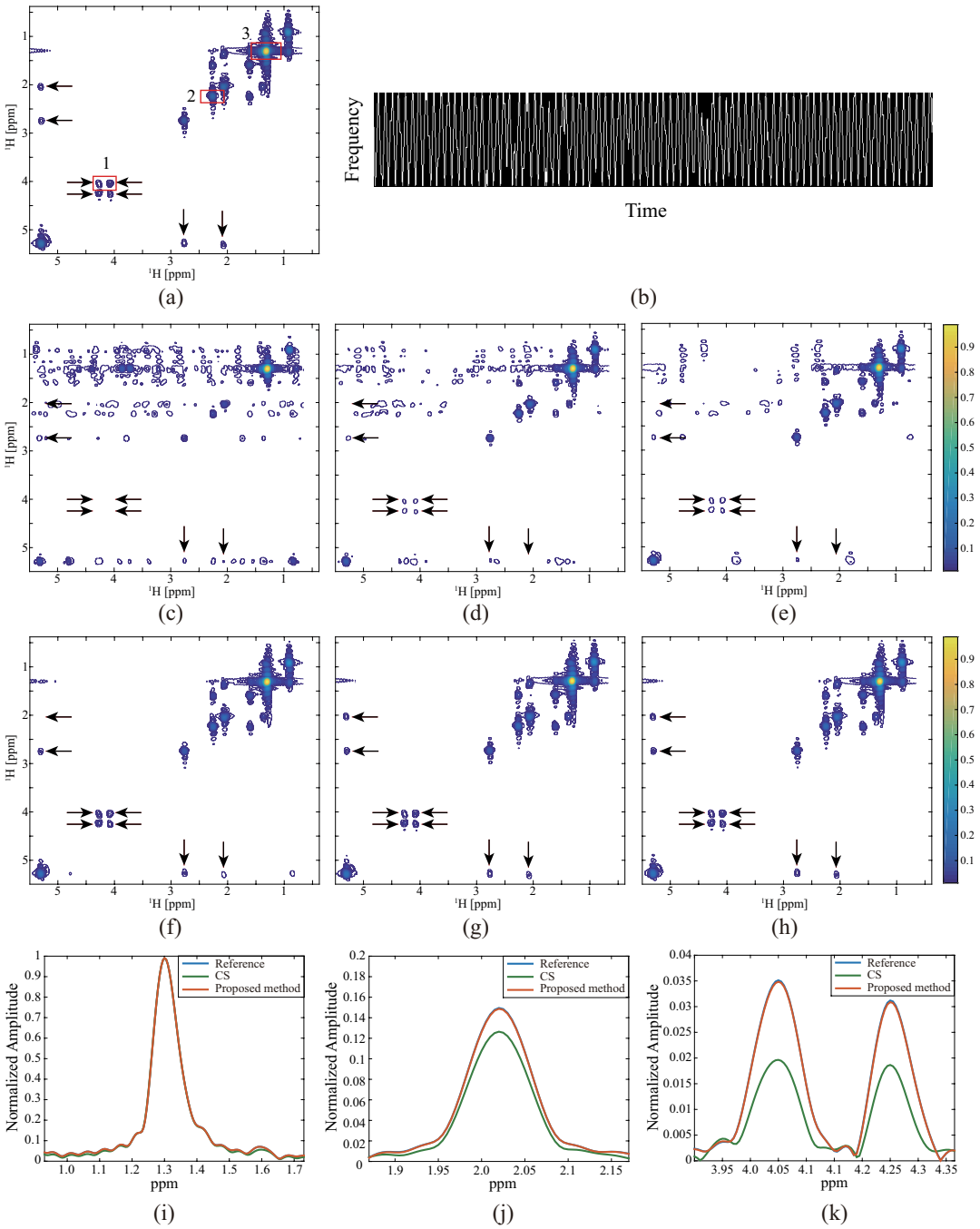

Fig. 11. Reconstructions of STEU COSY spectrum using gradient switching-based sampling pattern under different sampling rates. (a) denotes the fully sampled spectrum; (b) the gradient switching-based sampling pattern at sampling rate of 0.2; (c), (d) and (e) are the reconstructions by CS under sampling rates 0.2, 0.4 and 0.5, respectively; (f), (g) and (h) are the reconstructions by the proposed method under sampling rates 0.2, 0.4 and 0.5, respectively; (i), (j) and (j) are spectral line shapes of representative peaks #3, #2 and #1 (see (a) for peak positions) in (e) and (h). Note: The three peaks are with high, moderate and low intensities, respectively. The white points in sampling patterns denote the sampled data points while the black points denote the unsampled data points. The regularization parameter λ for the proposed method is 10^7.

[2] M. Betz *et al.*, "Biomolecular NMR: A chaperone to drug discovery," *Current Opinion in Chemical Biology*, vol. 10, no. 3, pp. 219–225, 2006.

[3] G. Topcu and A. Ulubelen, "Structure elucidation of organic compounds from natural sources using 1D and 2D NMR techniques," *Journal of Molecular Structure*, vol. 834-836, pp. 57–73, 2007.

[4] G. Hamilton *et al.*, "In vivo characterization of the liver fat ^{1}H MR spectrum," *NMR in Biomedicine*, vol. 24, no. 7, pp. 784–790, 2011.

[5] F. Cruz and S. Cerdán, "Quantitative ^{13}C NMR studies of metabolic compartmentation in the adult mammalian brain," *NMR in Biomedicine*, vol. 12, no. 7, pp. 451–462, 1999.

[6] A.-H. M. Emwas *et al.*, "NMR-based metabolomics in human disease diagnosis: Applications, limitations, and recommendations," *Metabolomics*, vol. 9, no. 5, pp. 1048–1072, 2013.

[7] J. Cavanagh *et al.*, *Protein NMR Spectroscopy*, 2nd ed. Burlington: Academic Press, 2007.

[8] M. Mobli and J. C. Hoch, "Nonuniform sampling and non-fourier signal processing methods in multidimensional NMR," *Progress in Nuclear Magnetic Resonance Spectroscopy*, vol. 83, pp. 21–41, 2014.

[9] H. Wang *et al.*, "Reduced data acquisition time in multi-dimensional NMR spectroscopy using multiple-coil probes," *Journal of Magnetic Resonance*, vol. 173, no. 1, pp. 134–139, 2005.

[10] E. Kupče and R. Freeman, "Fast multi-dimensional NMR of proteins,"

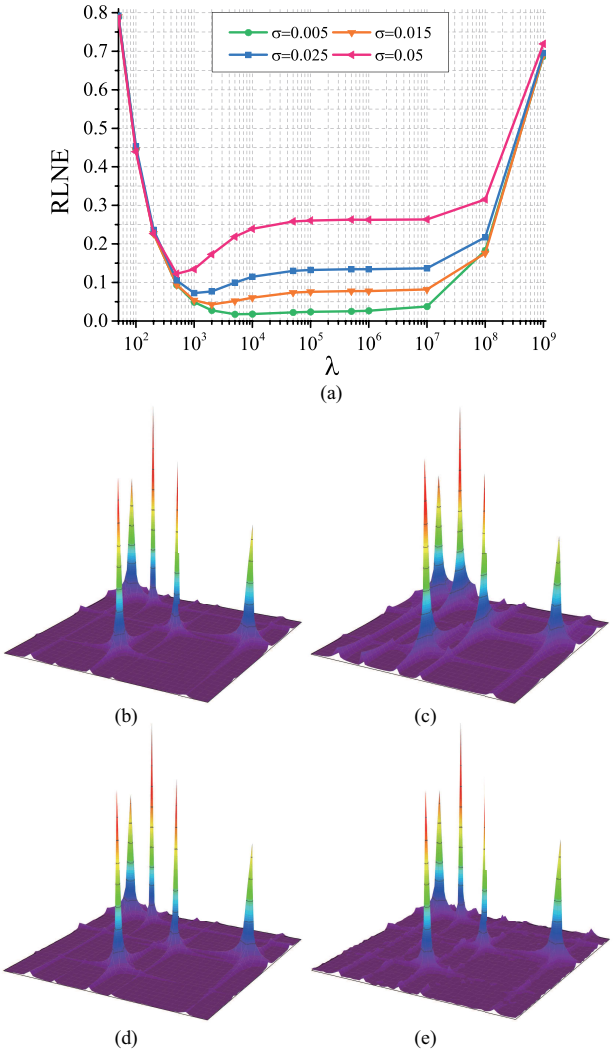

Fig. 12. Reconstructions with different regularization parameters λ. (a) Reconstruction errors (RLNE) versus regularization parameter λ under different noise levels, (b) denotes the noiseless ground-truth spectrum, (c)-(e) are reconstructed spectrum with $\lambda = 50$, 10^3 and 10^8, respectively. Note: The Poisson Gap sampling pattern with a sampling rate of 0.5 is adopted.

Journal of Biomolecular NMR, vol. 25, no. 4, pp. 349–354, 2003.

[11] Y. Shrot and L. Frydman, "Single-scan NMR spectroscopy at arbitrary dimensions," *Journal of the American Chemical Society*, vol. 125, no. 37, pp. 11 385–11 396, 2003.

[12] L. Frydman *et al.*, "The acquisition of multidimensional NMR spectra within a single scan," *Proceedings of the National Academy of Sciences*, vol. 99, no. 25, pp. 15 858–15 862, 2002.

[13] Z. Zhang *et al.*, "Spatially encoded ultrafast high-resolution 2D homonuclear correlation spectroscopy in inhomogeneous fields," *Journal of Magnetic Resonance*, vol. 227, pp. 39–45, 2013.

[14] B. E. Coggins and P. Zhou, "High resolution 4-D spectroscopy with sparse concentric shell sampling and FFT-CLEAN," *Journal of Biomolecular NMR*, vol. 42, no. 4, pp. 225–239, 2008.

[15] X. Qu *et al.*, "Compressed sensing for sparse magnetic resonance spectroscopy," in *18th Scientific Meeting on International Society for Magnetic Resonance in Medicine-ISMRM'10*, 2010, p. 3371.

[16] ——, "Reconstruction of self-sparse 2D NMR spectra from undersampled data in the indirect dimension," *Sensors*, vol. 11, no. 9, pp. 8888–8909, 2011.

[17] K. Kazimierczuk and V. Y. Orekhov, "Accelerated NMR spectroscopy by using compressed sensing," *Angewandte Chemie International Edition*, vol. 50, no. 24, pp. 5556–5559, 2011.

[18] D. J. Holland *et al.*, "Fast multidimensional NMR spectroscopy using compressed sensing," *Angewandte Chemie International Edition*, vol. 50, no. 29, pp. 6548–6551, 2011.

[19] X. Qu *et al.*, "Accelerated NMR spectroscopy with low-rank reconstruction," *Angewandte Chemie International Edition*, vol. 54, no. 3, pp. 852–854, 2015.

[20] J. Ying *et al.*, "Hankel matrix nuclear norm regularized tensor completion for N-dimensional exponential signals," *IEEE Transactions on Signal Processing*, vol. 65, no. 14, pp. 3702–3717, 2017.

[21] Z. D. Pardo *et al.*, "Monitoring mechanistic details in the synthesis of pyrimidines via real-time, ultrafast multidimensional NMR spectroscopy," *Journal of the American Chemical Society*, vol. 134, no. 5, pp. 2706–2715, 2012.

[22] P. Giraudeau *et al.*, "Ultrafast 2D NMR applied to the kinetic study of D-glucose mutarotation in aqueous solution," *Journal of Spectroscopy and Dynamics*, vol. 1, no. 2, pp. 2–7, 2011.

[23] Y. Shrot and L. Frydman, "Compressed sensing and the reconstruction of ultrafast 2D NMR data: Principles and biomolecular applications," *Journal of Magnetic Resonance*, vol. 209, no. 2, pp. 352–358, 2011.

[24] J. W. Yoon and S. J. Godsill, "Bayesian inference for multidimensional NMR image reconstruction," in *2006 14th European Signal Processing Conference*, Florence, Italy, 2006, pp. 1–5.

[25] A. S. Stern *et al.*, "NMR data processing using iterative thresholding and minimum ℓ_1-norm reconstruction," *Journal of Magnetic Resonance*, vol. 188, no. 2, pp. 295–300, 2007.

[26] É. Chouzenoux *et al.*, "Efficient maximum entropy reconstruction of nuclear magnetic resonance T1-T2 spectra," *IEEE Transactions on Signal Processing*, vol. 58, no. 12, pp. 6040–6051, 2010.

[27] R. J. Anderson *et al.*, *Organic Spectroscopic Analysis*. Royal Society of Chemistry, 2004.

[28] J. C. Hoch and A. S. Stern, *NMR Data Processing*. New York: Wiley-Liss, 1996.

[29] H. M. Nguyen *et al.*, "Denoising MR spectroscopic imaging data with low-rank approximations," *IEEE Transactions on Biomedical Engineering*, vol. 60, no. 1, pp. 78–89, 2013.

[30] G. Yang *et al.*, "Discrete wavelet transform-based whole-spectral and subspectral analysis for improved brain tumor clustering using single voxel MR spectroscopy," *IEEE Transactions on Biomedical Engineering*, vol. 62, no. 12, pp. 2860–2866, 2015.

[31] X. Qu *et al.*, "Accelerated magnetic resonance spectroscopy with vandermonde factorization," in *39th Annual International Conference of the IEEE Engineering in Medicine and Biology Society (EMBC 2017)*, 2017, accepted.

[32] H. Lu *et al.*, "A low rank hankel matrix reconstruction method for ultrafast magnetic resonance spectroscopy," in *39th Annual International Conference of the IEEE Engineering in Medicine and Biology Society (EMBC 2017)*, 2017, accepted.

[33] Y. Chen and Y. Chi, "Robust spectral compressed sensing via structured matrix completion," *IEEE Transactions on Information Theory*, vol. 60, no. 10, pp. 6576–6601, 2014.

[34] D. L. Donoho, "Compressed sensing," *IEEE Transactions on Information Theory*, vol. 52, no. 4, pp. 1289–1306, 2006.

[35] E. J. Candés *et al.*, "Robust uncertainty principles: Exact signal reconstruction from highly incomplete frequency information," *IEEE Transactions on Information Theory*, vol. 52, no. 2, pp. 489–509, 2006.

[36] Y. Hua, "Estimating two-dimensional frequencies by matrix enhancement and matrix pencil," *IEEE Transactions on Signal Processing*, vol. 40, no. 9, pp. 2267–2280, 1992.

[37] Y. Hua and T. K. Sarkar, "Matrix pencil method for estimating parameters of exponentially damped/undamped sinusoids in noise," *IEEE Transactions on Acoustics, Speech, and Signal Processing*, vol. 38, no. 5, pp. 814–824, 1990.

[38] J.-F. Cai. *et al.*, "A singular value thresholding algorithm for matrix completion," *SIAM Journal on Optimization*, vol. 20, no. 4, pp. 1956–1982, 2010.

[39] N. Halko *et al.*, "Finding structure with randomness: Probabilistic algorithms for constructing approximate matrix decompositions," *SIAM Review*, vol. 53, pp. 217–288, 2011.

[40] K. Mohan and M. Fazel, "Iterative reweighted algorithms for matrix rank minimization," *Journal of Machine Learning Research*, vol. 13, pp. 3441–3473, 2012.

[41] K. Konishi *et al.*, "Iterative partial matrix shrinkage algorithm for matrix rank minimization," *Signal Processing*, vol. 100, pp. 124–131, 2014.

[42] N. Srebro, "Learning with matrix factorizations," Ph.D. dissertation, Massachusetts Institute of Technology, 2004.

[43] S. Boyd *et al.*, "Distributed optimization and statistical learning via the alternating direction method of multipliers," *Foundations and Trends® in Machine Learning*, vol. 3, no. 1, pp. 1–122, 2011.

[44] X. Qu *et al.*, "Magnetic resonance image reconstruction from undersampled measurements using a patch-based nonlocal operator," *Medical Image Analysis*, vol. 18, no. 6, pp. 843–856, 2014.
[45] S. G. Hyberts *et al.*, "Poisson-Gap sampling and FM reconstruction for enhancing resolution and sensitivity of protein NMR data," *Journal of the American Chemical Society*, vol. 132, no. 7, pp. 2145–2147, 2010.
[46] M. R. Smith *et al.*, "In vivo imaging and spectroscopy of dynamic metabolism using simultaneous ^{13}C and ^{1}H MRI," *IEEE Transactions on Biomedical Engineering*, vol. 59, no. 1, pp. 45–49, 2012.
[47] O. A. Ahmed, "New denoising scheme for magnetic resonance spectroscopy signals," *IEEE Transactions on Medical Imaging*, vol. 24, no. 6, pp. 809–816, 2005.
[48] M. Jacob *et al.*, "Improved model-based magnetic resonance spectroscopic imaging," *IEEE Transactions on Medical Imaging*, vol. 26, no. 10, pp. 1305–1318, 2007.
[49] A. G. Christodoulou *et al.*, "Improved subspace estimation for low-rank model-based accelerated cardiac imaging," *IEEE Transactions on Biomedical Engineering*, vol. 61, no. 9, pp. 2451–2457, 2014.
[50] Y. Yang *et al.*, "Aliasing artefact suppression in compressed sensing MRI for random phase-encode undersampling," *IEEE Transactions on Biomedical Engineering*, vol. 62, no. 9, pp. 2215–2223, 2015.
[51] Z. Zhan *et al.*, "Fast multiclass dictionaries learning with geometrical directions in MRI reconstruction," *IEEE Transactions on Biomedical Engineering*, vol. 63, no. 9, pp. 1850–1861, 2016.